Fatigue Strength and Fracture Mechanisms in the Very-High-Cycle-Fatigue Regime of Automotive Steels

Mohamed Sadek,* Jens Bergström, Nils Hallbäck, Christer Burman, Roberto Elvira, and Borja Escauriaza

Very-high-cycle-fatigue (VHCF) strength properties are of interest to several technical applications assessed globally at different laboratories with long-life fatigue testing capabilities. Also, VHCF failure mechanisms are a scientific topic with remaining open research questions. Herein, three automotive bar grade steels are studied with respect to VHCF strength and initiation mechanisms. A microalloyed ferritic–pearlitic steel (38MnSiV5, 870 MPa tensile strength), a quenched and tempered martensitic steel (50CrV4, 1410 MPa tensile strength), and a carburizing steel (16MnCr5, 1180 MPa core structure tensile strength) are studied to reveal characteristics regarding initiation and VHCF failure mechanisms. A 20 kHz ultrasonic fatigue testing instrument is used to obtain fatigue lives up to and above 10^9 load cycles in uniaxial loading. Hour-glass specimens, smooth or notched, are tested at $R = -1$ and $R = 0.1$. Fatigue strength and stress life (SN)-diagram data are achieved, and crack initiation and growth mechanisms are studied using primarily field-emission gun–scanning electron microscopy (FEG–SEM). Fatigue strengths are explained by a modified life-dependent Murakami-expression, the Haigh diagram, and notch sensitivity. Interior and surface crack initiations by surface defects, triple points, and inclusions are found. The fine granular area (FGA) to fish-eye crack growth transition conditions are explored and schematic descriptions are given.

1. Introduction

With the large variety of different steel alloys and steel conditions being used in automotive manufacturing, the mapping of properties is important for the selection of steel alloy

Dr. M. Sadek, Prof. J. Bergström, Dr. N. Hallbäck, Dr. C. Burman
Department of Engineering and Physics
Karlstad University
Karlstad SE-658 88, Sweden
E-mail: mohamed.sadek@kau.se

Dr. R. Elvira, Dr. B. Escauriaza
Department of Development of New Products
SIDENOR I+D
S.A., Barrio Ugarte s/n, Basauri E-48970, Spain

The ORCID identification number(s) for the author(s) of this article can be found under https://doi.org/10.1002/srin.202000060.

and design of components. High-strength martensitic bar grades and high-strength low-alloy steels are frequently used in automotive applications, as in drive lines and engine parts, e.g., carburized steels in gear applications. Many of the automotive components are commonly subjected to cyclic loading, and the vehicle performance is determined by fatigue properties. Thus, it motivates studies of automotive steels under, e.g., very-high-cycle-fatigue (VHCF) conditions.[1–3]

The classic stress life (SN) curve, **Figure 1**a, drawn by August Wöhler was limited to $N = 10^6$ cycles and assumed the stress limit for infinite fatigue life at this point. The failure mechanism for specimens failing in the low-cycle-fatigue and high-cycle-fatigue (LCF and HCF) regime was predominantly surface crack initiations.[4] However, in the past decades, new failure mechanism and fatigue crack initiation processes (influences of internal/external defects, types of defects, and detailed initiation mechanisms) related to the VHCF regime were treated and the classic Wöhler curve was extended, as shown in Figure 1b.[5–8] Particularly, as in VHCF, the major part of the fatigue life is spent during initiation. The initiation processes become more critical and have been studied in more detail.[9–17] Due to the development and use of ultrasonic fatigue testing instruments, the VHCF regime is reached in a reasonably short time (with 20 kHz load frequency, 10^9 cycles are reached within 14 h). Consequently, the number of laboratories installing and using an ultrasonic fatigue testing instrument have been increasing.[18]

Several different test specimen geometries are used in fatigue testing depending on the test requirements.[19,20] Common test geometries include smooth and notched specimens and different specimen sizes. Stress gradients and effectively stressed volumes can be quite dissimilar depending on specimen geometry, affecting the test outcome. If there is an associated critical defect distribution which initiates failure, these factors have to be considered.[21,22] Of special interest in fatigue data for engineering purposes is the influence of mean stress and the presence of notches in components.

It has been shown through studies that the failure mechanisms in region III for high-strength martensitic steels are often due to nonmetallic inclusions. When internal fatigue failure
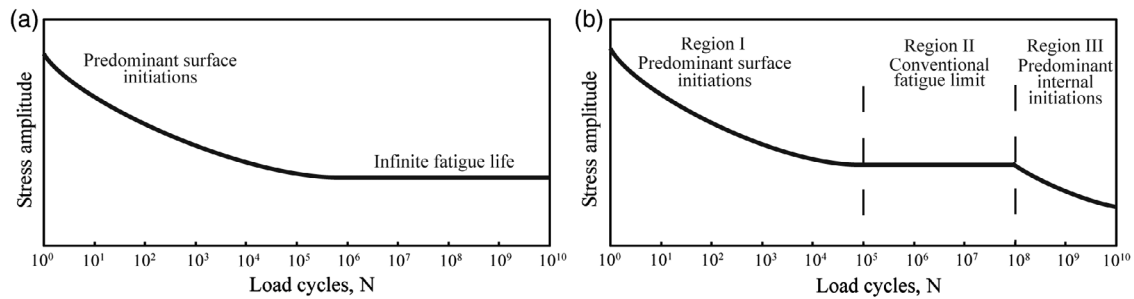
Figure 1. a) The Wöhler SN curve and b) the SN curve including the VHCF regime.

occurs in the VHCF regime, an area named optically dark area (ODA) may be observed around the initiation site. Within this area, a fine granular topographic structure is observed and hence the alternative designation fine granular area (FGA) was established. Outside the FGA/ODA, the fracture surface displays a flat appearance which constitutes the fish eye. Further, outside the fish eye the fatigue crack continues until the final fracture is reached. Murakami introduced a formula, Equation (1), relating the fatigue strength at 10^7 cycles of a material to the size of the ODA, mechanical strength of the material, and the loading ratio.[23–25]

$$\sigma_{FL} = A \frac{(HV + 120)}{\sqrt{area_{ODA}}^{1/6}} \left(\frac{1 - R}{2}\right)^{\alpha} \quad (1)$$

The constant A is 1.43 and 1.56 for surface and subsurface crack initiations, respectively, and $\alpha = 0.226 + HV \ 10^{-4}$. As mentioned, the fatigue limit (σ_{FL}) in Equation (1) is at a specific fatigue life, i.e., a number of load cycles. Wanting to take the fatigue life (N_f) into account, Bathias[18] modified Equation (1) by replacing the constant A with $\beta = \beta_1 - \beta_2 \ln(N_f)$, see Equation (2). The constants $\beta_1 = 3.09$ and $\beta_2 = 0.12$ are found to be fitting for the specific types of materials tested.

$$\sigma_{FL} = \beta \frac{(HV + 120)}{\sqrt{area}^{1/6}} \left(\frac{1 - R}{2}\right)^{\alpha} \quad (2)$$

In the present study, results of different specimen geometries, hourglass-shaped smooth and notched specimens, used in VHCF testing are presented. Stress distributions computed by dynamic finite-element method (FEM) calculations display the effect of specimen geometries. Test results of smooth and notched specimens, $K_t = 1.4$, and mean stress effects, $R = 0.1$ and $R = -1$, are shown in SN diagrams in the life range of 10^6–10^9 load cycles.

2. Experimental Section

2.1. Materials

Three high-strength bar steel grades were investigated in the present study and test specimens were sampled and prepared along the rolling direction of a Ø60 mm bar steel billet, and the chemical composition is shown in **Table 1**. 38MnSiV5 is a ferritic–pearlitic microalloyed steel, in which the normal contents of oxides and sulphide inclusions were observed.

Table 1. Chemical composition of the tested steel grades, wt%.

Grade	C	Mn	Si	P	S	Cr	Ni	Mo	V
38MnSiV5	0.37	1.46	0.68	0.011	0.050	0.12	0.10	0.03	0.10
50CrV4	0.52	0.87	0.33	0.009	0.003	1.08	0.09	0.03	0.11
16MnCr5	0.16	1.10	0.27	0.011	0.021	1.02	0.11	0.03	0.01

50CrV4 is a high-strength steel, austenitized at 850 °C/30 min, oil quenched followed by tempering at 500 °C/1 h, and after specimen manufacturing, it achieved the highest tensile strength with tempered martensite found in the microstructure. 16MnCr5 grade contained a relatively higher content of small-sized oxides and sulphides, to improve machinability, and was carburized to obtain a martensitic microstructure with a hardened surface layer with 5% retained austenite. Core properties were obtained using test specimens, heat treated by the carburizing heat-treatment cycle at 900 °C/3.5 h and 860 °C/2.5 h, oil quenched to 80 °C, and tempered at 160 °C/2 h.

The microstructures of the three steel grades are shown in **Figure 2**. The two-phase ferritic–pearlitic microstructure of the 38MnSiV5 steel grade is shown in Figure 2a, the fine martensitic needle-like structure of 50CrV4 in Figure 2b, and the core microstructure, tempered martensite with some bainite and ferrite of the carburized steel grade 16MnCr5, in Figure 2c.

Grain size measurements of the three steel grades were carried out on etched specimens. Nital 5% etch was enough to reveal the grain boundaries in the ferritic–pearlitic steel (38MnSiV5), whereas for the two martensitic steels (50CrV4 and 16MnCr5) an alternative picral etch was required. Thus, perlite and ferrite grain sizes and prior austenite grain sizes were obtained, as shown in **Table 2**.

The mechanical properties of the steel grades are shown in **Table 3**. However, the mechanical properties of the carburized 16MnCr5 grade are present in core heat-treated specimens. The hardness profile of the carburized specimens is shown in **Figure 3**. The dashed lines indicate a carburized case depth of 0.6 mm.

2.2. Experimental Method

A 20 kHz ultrasonic fatigue test instrument (a pulse generator, an oscillator, and a magnifying horn) was used to conduct the fatigue tests in this work. To enable the static load the whole system was mounted in a tensile test screw machine.
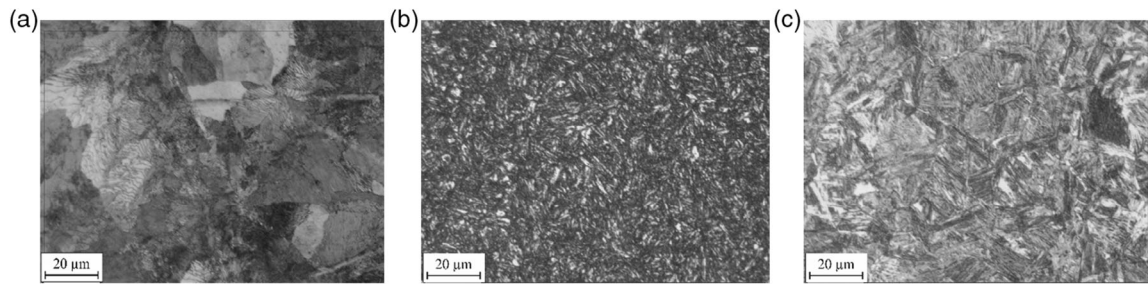
Figure 2. Microstructure of a) 38MnSiV5 grade, b) 50CrV4 grade, and c) core microstructure of the 16MnCr5 grade.

Table 2. Average grain sizes of the three steel grades.

Grade	38MnSiV5	50CrV4	16MnCr5
Diameter [µm]	4.9	4.0	4.4

Table 3. Mechanical properties.

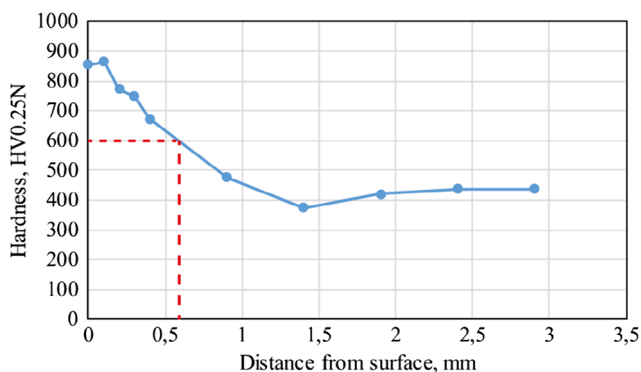| Grade	Direction	Tensile strength [MPa]	Yield strength [MPa]	Elongation [%]	Area reduction [%]	Hardness [HV30kg]
38MnSiV5	Rolling	867	589	20	55	267
50CrV4	Rolling	1409	1333	13	51	435
16MnCr5[a]	Rolling	1175	876	9.4	34	380

[a]Core properties for 16MnC.

Figure 3. Vickers hardness profile of the carburized 16MnCr5 grade, measured with a 0.25 N load.

The effect of mean load was investigated using two mean load ratios, $R = -1$ and $R = 0.1$, and the notch effect was studied by preparing notched specimens with a geometrical stress concentration factor $K_t = 1.44$. The specimen stresses were computed using dynamic simulations at resonance frequency modeled in the FEM software Abaqus. Stress distributions in the specimens with a prescribed 10 µm displacement at the specimen ends are shown in **Figure 4**c,d.

Smooth and notched hourglass specimen geometries were designed to run at resonance in a 20 kHz ultrasound fatigue test machine with a net section diameter of 4.0 mm, a notch depth of 1.0 mm, and a notch radius of 2.0 mm, as shown in Figure 4a,b. The test specimens were all prepared to their geometry, heat treated to final hardness, and the 38MnSiV5 and 50CrV4 were subsequently prepared by fine grinding and polishing to final surface finish. 16MnCr5 was prepared to final surface finish prior to carburizing to maintain the carburized layer and surface properties.

Water cooling was used for the $R = -1$ tests and pressurized under air cooling for the $R = 0.1$ tests. To ensure that there was no overheating in the $R = 0.1$ testing, where water cooling was not possible but where undercooled air was used, the specimen surface temperature was measured during fatigue testing. The measured temperatures were always below 45, 50, and 35 °C for 38MnSiV5, 50CrV4, and 16MnCr5 grades, respectively.

For each material, loading condition, and specimen type, 15 specimens were included in a staircase test to determine the fatigue strength at 10^8 cycles.[26] In such testing, the first specimen was tested at a stress level slightly higher than the estimated mean fatigue strength. If the specimen failed prior to the cutoff lifetime, the next specimen was tested at a lower stress level. If the specimen survived, i.e., a "run-out," then the next specimen was tested at a higher stress level. The increments were usually around 5% of the mean fatigue strength. For data reduction the Dixon–Mood[27] technique was applied to evaluate the statistical test outcome. The method was based on the maximum likelihood estimation method and assumed a normal distribution of the fatigue strength.

Additional 15 specimens, of each subgroup, were tested at three different stress levels to produce data for the SN curves, in the 10^6–10^{10} cycle regime. A common way to evaluate an SN curve was the standardized linear fatigue response, modeled according to Equation (3).[28]

$$\mathrm{Log}_{10}(N) = b_0 + b_1 \mathrm{Log}_{10}(S) \tag{3}$$

Test statistics, regression coefficients, and standard deviations were evaluated according to the SS-ISO 1207 standard.[28]

Temperature measurements were carried out during the $R = 0.1$ tests, using an infrared thermal imaging camera. Fractography of the failed specimens was conducted using field-emission gun–scanning electron microscopy (FEG-SEM), a LEO scanning electron microscope. The initiation mechanism, defect size and location, FGA size, fish-eye size, and the chemical content of any internal defects were determined.

In an attempt to understand the phenomena behind the transitions from FGA formation to fish-eye growth and from fish-eye
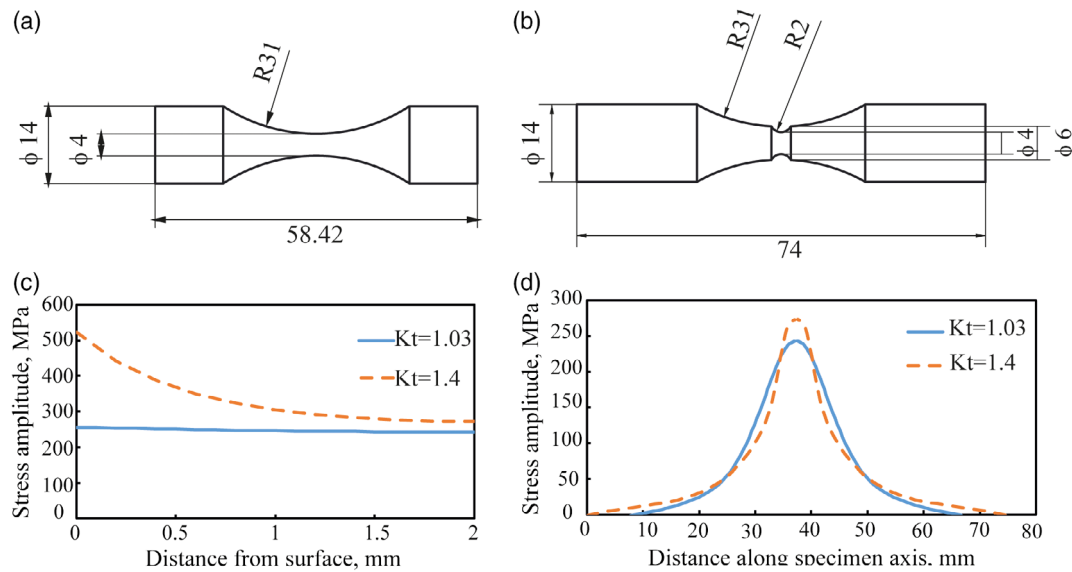
Figure 4. a) Smooth specimen geometry ($K_t = 1.03$), b) notched specimen geometry ($K_t = 1.44$), c) longitudinal stress distribution along the cross section of the specimens midsection, and d) longitudinal stress distribution along the specimen center line.

growth to final crack growth, the stress intensity factor and Irwin's plastic zone size were calculated at the boundaries of the mentioned. The stress intensity factor was calculated according to Equation (4) and the Irwin plastic zone, r_p, according to Equation (5).[29,30]

$$K_I = Y\sigma\sqrt{a\pi} \tag{4}$$

where the geometry function Y is $2/\pi$ for a circular interior crack and σ is σ_{max} at $R = 0.1$ and $R = -1$ ratios. a is the radius of the specific feature, (a_{inc}, a_{FGA}, or $a_{fish\ eye}$). The plastic zone radius r_y may be written as

$$r_y = \frac{r_p}{2} = \frac{1}{6\pi}\left(\frac{K_I}{\sigma_{ys}}\right) \text{ (plain strain)} \tag{5}$$

3. Results

The staircase fatigue testing method with upper limit at 10^8 cycles provides the fatigue strength data shown in **Table 4**. The values presented correspond to the local stresses at the specimen surface.

The fatigue strength is expected to decrease with an increased mean load. This effect is clearly shown in the results of 38MnSiV4 and 16MnCr5 grades, as shown in Table 4 and **Figure 5** and **6**. On some of the 50CrV4 grade specimens, surface

Table 4. Fatigue strength at 10^8 cycles and standard deviation for different loading conditions in local stress amplitudes, MPa.

Load ratio	Notch factor	38MnSiV5	50CrV4	16MnCr5
$R = -1$	$K_t = 1.03$	343 ± 6	558 ± 15	677 ± 33
$R = 0.1$	$K_t = 1.03$	258 ± 4	543 ± 6	402 ± 20
$R = -1$	$K_t = 1.4$	339 ± 16	650 ± 26	598 ± 15

defects were observed. Therefore, in Figure 5 and 6, only specimens with interior initiated cracks are presented to eliminate the effect of surface defects. However, for the 50CrV4 grade, the decrease in the fatigue strength with mean load is not pronounced, hence the position shift between the 50CrV4 and 16MnCr5 grades in Figure 5 and 6. The fatigue test results of the notched specimens are shown in **Figure 7**, following the orders of stress levels as the smooth test series in Figure 6. Further, the SN data clearly reveal a low sensitivity of fatigue strength to the cyclic life in the life range of 10^6–10^9 cycles, revealed by the flat appearance of the SN curves.

The results in Table 4 are as well presented in a Haigh diagram in **Figure 8**, where the fatigue strength results of 38MnSiV4 and 16MnCr5 grades are in good agreement with the Goodman fatigue strength—mean stress relation model. But the 50CrV4 grade data point at $R = -1$ deviates significantly from the Goodman relationship line.

Fractography of the failed specimens was conducted using a high-resolution LEO FEG–SEM. The causes for initiation and defect size, location, and chemical content were determined. The analysis revealed both surface and subsurface crack initiation sites. The subsurface initiations started at triple points in the 38MnSiV5 grade with the formation of FGA and fish-eye features around the initiation site, as shown in **Figure 9**. In the 50CrV4 and 16MnCr5 grades, the subsurface initiations started at nonmetallic inclusions, also with formation of FGA and fish-eye features, however, more typical for martensitic steel grades, as shown in **Figure 10** and **11**. The results of the $R = -1$ testing of the $K_t = 1.03$ specimens revealed the crack initiation sites to be mostly at the surface for the 38MnSiV5 grade, exclusively on the surface for 50CrV4 grade and 50/50 surface/subsurface for the 16MnCr5 grade. Increasing the mean load to $R = 0.1$ had no effect on the crack initiation site distribution for the 38MnSiV5 and 16MnCr5 grades, whereas for the 50CrV4 grade approximately half of the failed specimens showed interior crack
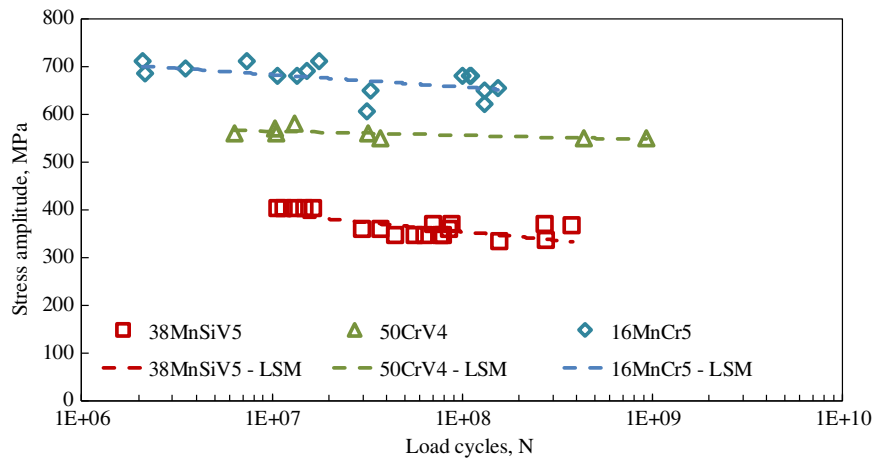
ADVANCED
SCIENCE NEWS
www.advancedsciencenews.com

steel
research
international
www.steel-research.de

Figure 5. SN curves and least square method fitting for the three steel grades. $R = -1$ and $K_t = 1.03$.
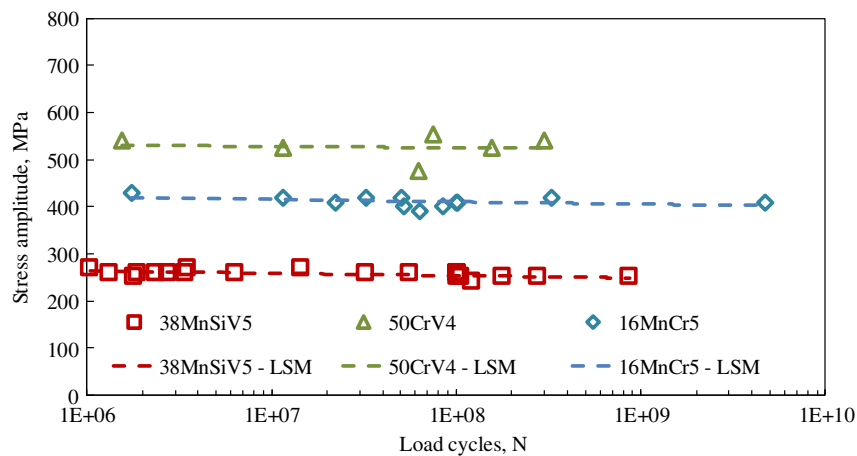

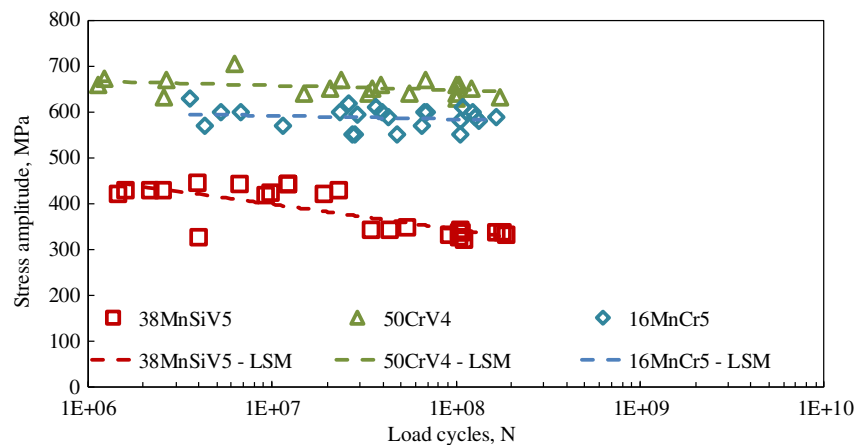**Figure 6.** SN curves and least square method fitting for the three steel grades. $R = 0.1$ and $K_t = 1.03$.

Figure 7. SN curves and least square method fitting for the three steel grades. $R = -1$ and $K_t = 1.44$.

initiation sites. All the notched specimens failed at the surface, in accordance with the stress gradient below the notch, except a few specimens of the carburized 16MnCr5 grade where crack initiation sites were found close to the surface.

As mentioned, many of the smooth specimens, $K_t = 1.03$, failed by subsurface crack initiations. This type of initiation normally creates the well-known fish-eye feature on the fracture surface, as clearly shown in the fractography analysis. It was noticed
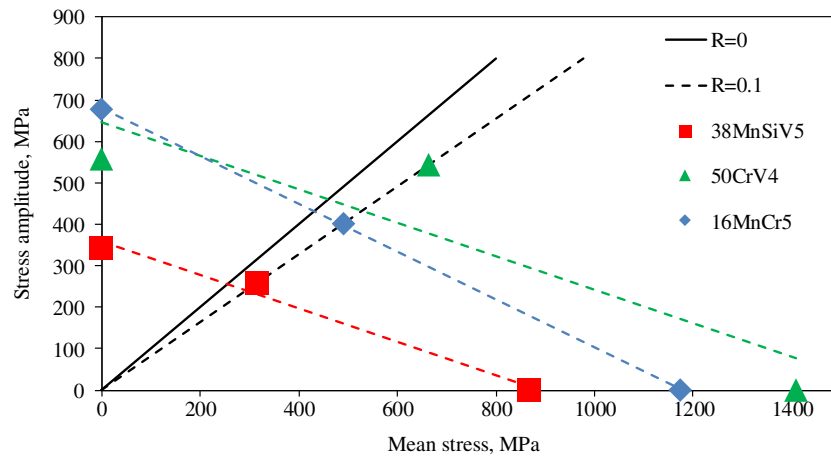
**ADVANCED
SCIENCE NEWS**

www.advancedsciencenews.com

**steel
research**
international

www.steel-research.de

Figure 8. Goodman relationship fitted to the fatigue strength results presented in a Haigh diagram.
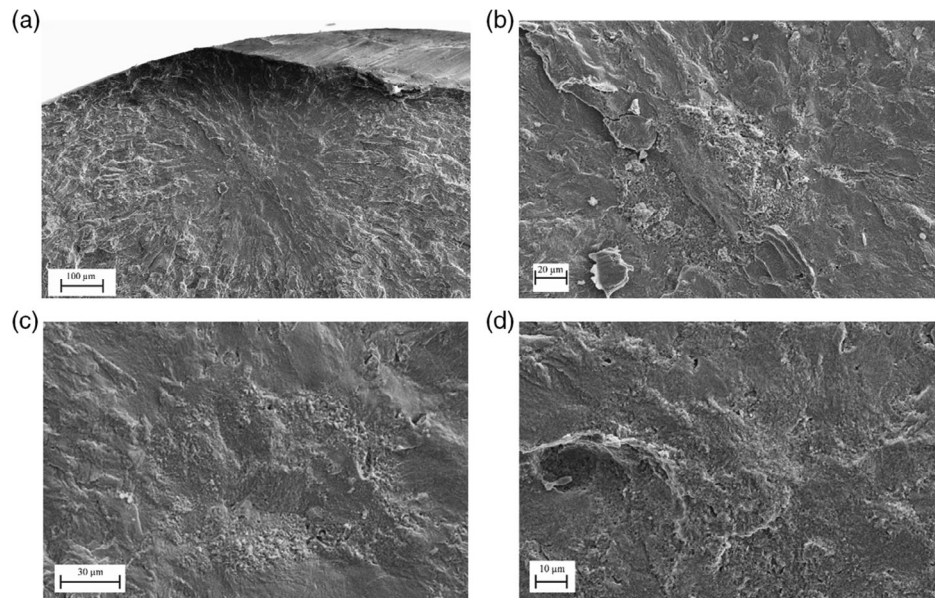

Figure 9. a) Overview and b) close-up of FGA and fish-eye formation around the crack initiation point in the 38MnSiV5 grade. $\sigma_a = 250$ MPa and $N = 8.67 \times 10^8$. FGA formation in two different specimens at $\sigma_a = 250$ MPa, c) $N = 2.78 \times 10^8$, and d) $N = 1.78 \times 10^8$.
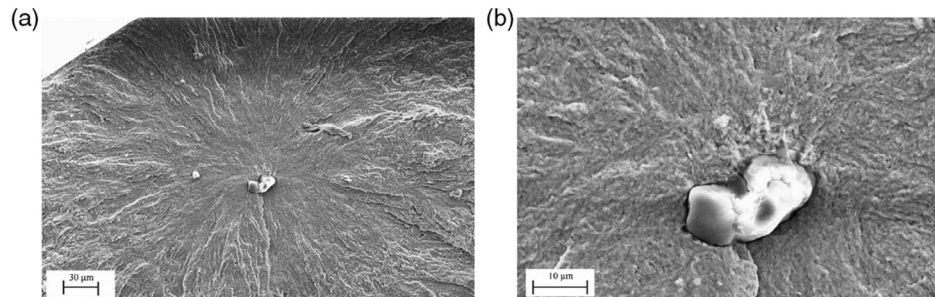

Figure 10. a) Overview and b) close-up of FGA and fish-eye formation around a nonmetallic inclusion at the crack initiation point in the 50CrV4 grade, $\sigma_a = 555$ MPa and $N = 7.5 \times 10^7$.

that the size of the fish-eye region varied from one specimen to another and from one steel grade to another. An analysis of data displayed an effect of the material strength on the size of the fish-eye region. The hardness profiles of the three steel grades and the
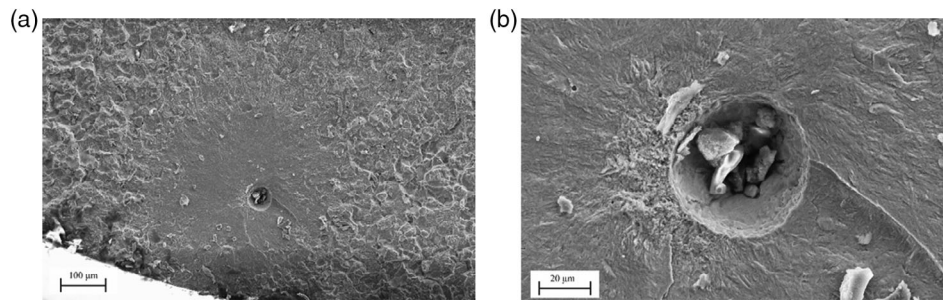
**ADVANCED
SCIENCE NEWS**

www.advancedsciencenews.com

**steel
research**
international

www.steel-research.de

Figure 11. a) Overview and b) close-up of FGA and fish-eye formation around an inclusion at the crack initiation point in the 16MnCr5 grade. $\sigma_a = 410$ MPa and $N = 4.74 \times 10^9$.

calculated stress intensity factors of measured fish-eye sizes, in Equation (4), at $R = 0.1$ and $R = -1$ load ratios, respectively, are shown in **Figure 12**. It is clear that the change in material strength, hardness in this case, coincides with a change in stress intensity at the fish-eye border. The carburized layer of the 16MnCr5 grade results in an increased hardness toward the surface, as shown in Figure 3 and 12. The related stress intensity estimated at the fish-eye border is much higher when the crack is initiated at a higher hardness close to the surface.

The transformation from the FGA formation to a more flat crack growth within the fish eye is assumed to occur when the stress intensity factor at the crack tip reaches a material-specific threshold value. The size of the FGAs is expected to increase with increasing fatigue life. Taking the load amplitude into account, i.e., calculating the stress intensity factor at the measured FGA border, it is observed that the ΔK_{FGA} is relatively

constant along the fatigue life. Note that the crack size at the FGA border is assumed as the sum of the initiation defect and FGA sizes.

The FGA sizes measured on the fracture surfaces of the three automotive steel grades plotted against fatigue life in **Figure 13** increase somewhat with fatigue life. The effective stress intensity (Mode I) at the FGA border is plotted against fatigue life, as shown in **Figure 14**, where the dashed lines indicate the average FGA border stress intensities assumed to be related to material-specific threshold values. The indicated values for $R = 0.1$ are 4.4, 4.9, and 5.0 MPa$\sqrt{m}$ for 38MnSiV5, 50CrV4, and 16MnCr5 steel grades, respectively. For $R = -1$, the indicated values are 2.3 and 3.6 MPa$\sqrt{m}$ for 38MnSiV5 and 16MnCr5 steel grades, respectively.

The crack tip plastic zone and its relation to the surrounding microstructure is the one controlling parameter of crack growth.
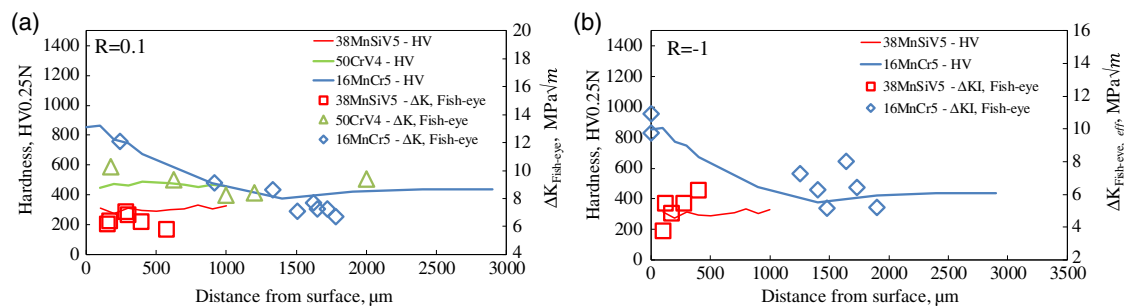

Figure 12. Hardness and fish-eye stress intensity of the three steel grades at a) $R = 0.1$ and b) $R = -1$ loading ratios.
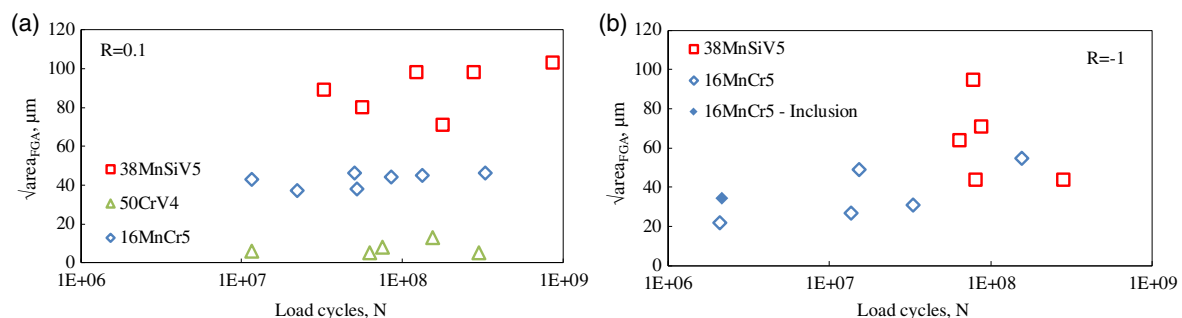

Figure 13. Size of FGA against cycles to failure for a) $R = 0.1$ and b) $R = -1$ loading ratios.

**ADVANCED
SCIENCE NEWS**
www.advancedsciencenews.com

**steel
research**
international
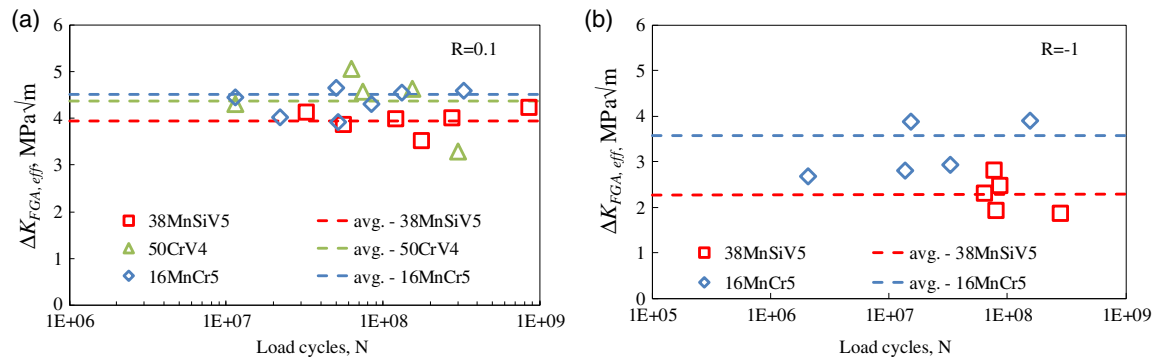www.steel-research.de

Figure 14. Stress intensity factor at FGA border ($\Delta K_{FGA, eff} = K_{max}$-0) plotted against fatigue life for a) $R = 0.1$ and b) $R = -1$ loading ratios.

Therefore, the Irwin plastic zone was calculated at the borders of both the FGA and the fish-eye area of all fracture surfaces, according to Equation (5), using the maximum stress intensity factor K_{max}. An increasing $\sqrt{area}$ versus r_p relation at the fish-eye and FGA borders, respectively, was found, as shown in **Figure 15** and **16**. The linear response demonstrated is expected given the relationship between the $\sqrt{area}$ parameter and the Irwin plastic zone, r_p, in Equation (4) and (5), where the sizes of the FGA's and fish eyes are measured with SEM.

There is a clear order of the measured FGA sizes between the three different steel grades studied here. In an attempt to understand the reason behind this effect, an investigation was conducted to find a "limiting material unit" ("LMU") beyond which no effect of the microstructural variation on the mechanical properties of the material exists. A relatively straight-forward way to investigate this is by measuring the Vickers hardness ("HV"), using varying loads and studying the indent area effect on the HV dispersal. The successive increase in the indent area yields a successive decrease in the HV standard deviation as microstructural variations are encompassed by larger plastic flow zones around the indent. Standard Vickers instruments were used and with applied loads in the range of 0.05–500 N. **Figure 17** shows the ratio $HV_{standard\ deviation}/HV_{average}$, representing the HV variability, for the three steel grades at different indent average diagonals (i.e., applied loads). The three steel grades are seen to a level of low HV variability at different indent diagonal sizes, the smallest and highest indent sizes for the 50CrV4 and 38MnSiV5 grades, respectively.
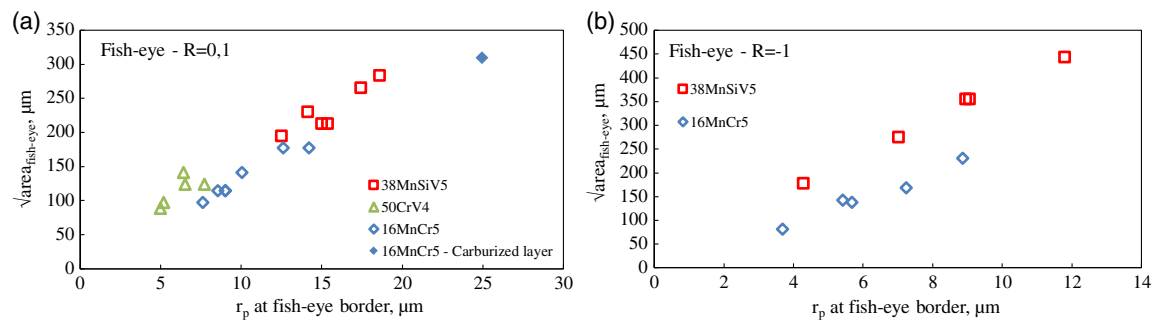

Figure 15. Fish-eye area versus Irwin plastic zone size r_p at the fish-eye border for a) $R = 0.1$ and b) $R = -1$.
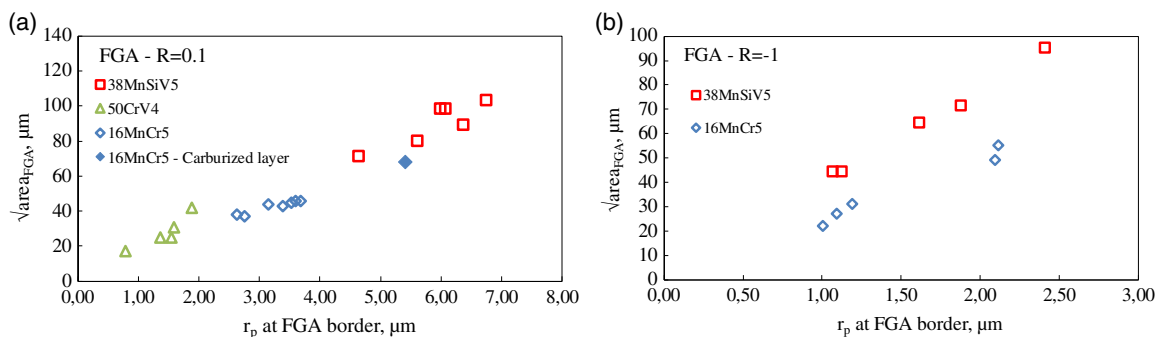

Figure 16. FGA area versus Irwin plastic zone size r_p at the FGA border for a) $R = 0.1$ and b) $R = -1$.
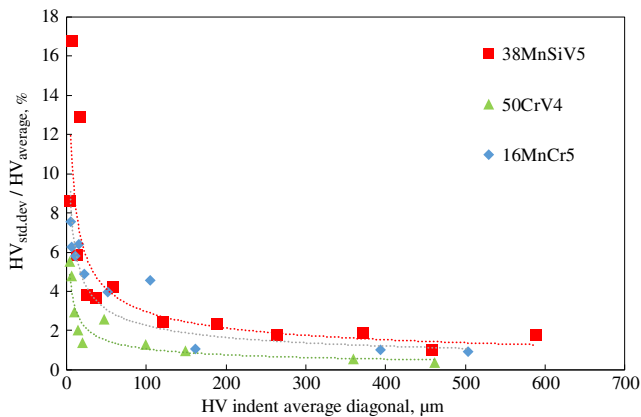
Figure 17. Relative HV variability versus HV indent diagonal average.

4. Discussion

An increase in the mean load, i.e., a higher R ratio, expectedly results in a decrease in the fatigue strength, as shown in Figure 8. The fatigue strength decreases with higher R values for the 38MnSiV5- and 16MnCr5 grades, as shown in Table 4 and Figure 5 and 6. However, the 50CrV4 grade shows only a very small decrease in fatigue strength. For the smooth specimens, $K_t = 1.03$, the initiation sites are expected to be divided between the surface and interior whereas for the notched specimens, $K_t = 1.44$, all initiation sites should be located at, or close to, the surface because of the much higher local stresses at the surface, as shown in Figure 4c. The SEM fracture surface analysis confirms this effect for 38MnSiV5 and 16MnCr5 grades. However, the 50CrV4 initiation sites were located on the surface, for both $K_t = 1.03$ and $K_t = 1.44$. Thus, the $R = -1$ fatigue strength of the 50CrV4 grade is assumed to be reduced from an optimal level due to the surface defects. Indeed, as shown in Figure 8, a significantly higher, $\approx 50\%$, fatigue strength at $R = -1$ of the 50CrV4 grade can be predicted.

An analysis of the notch effect may initially be visualized by the notch factor in fatigue, K_f, in relation to the geometrical stress concentration $K_t = 1.4$. The notch factor in fatigue is defined as the ratio of the fatigue strength of smooth specimens to fatigue strength of notched specimens and is dependent on the notch radius and the material notch sensitivity. The experimental fatigue strengths obtained give $K_f = 1.4$, 1.2, and 1.6 for 38MnSiV5, 50CrV4, and 16MnCr5, respectively. It may be interpreted as being reasonable for 38MnSiV5, low because of the influence of inferior surfaces for 50CrV4 and high because of enhanced defect sensitivity of the carburized layer for 16MnCr5.

The influence of the high load frequency on the fatigue properties has been investigated in a previous study[2] where the three steel grades were tested using different load frequencies (1, 150, 1000, and 20 000 Hz). The results showed good agreement between the results of different load frequencies and hence the frequency effect is presumed insignificant. However, during high load frequency testing, there is in certain cases a risk of heating of the test specimen due to internal friction. The $R = 0.1$ tests of the $K_t = 1.03$ specimens are expected to cause the highest elevated temperatures because of the larger, relative

to the notched specimens, midsection volume and the higher maximal stresses. For that reason, the temperature measurements presented earlier are the highest during these tests, and the 35–50 °C levels are of minor influence. At the final fracture phase, during crack propagation to final fracture, localized heating may occur.[3] Also, localized hot spots in the final fracture phase have been reported.[9,10] However, the final fracture phase constitutes only a small fraction of the total life in VHCF,[11–13] so there is limited influence on total life and fatigue strength.

The effect of the inclusion size on fatigue life was analyzed with the results of the martensitic 50CrV4 steel grade in $R = 0.1$ testing, as shown in **Figure 18**. A trend is observed, although, with little amount of data, where the decrease in the inclusion size corresponds to an increase in fatigue life. The stress intensity factor at the inclusion/defect border (ΔK_{inc}) is expected to decrease with increasing fatigue life, as shown in Figure 18. These presumptions have been confirmed by several researchers.[14,15,23,31] In effect, the inclusion or defect size will influence the fatigue strength and fatigue life.

As mentioned earlier, Bathias[18] modified Murakami's model[23–25] to introduce the dependency of fatigue life, as shown in Equation (2). Bathias model was applied on the present fatigue test results and plotted with reference to the model curve, as shown in **Figure 19**a,b. However, to bring the data points closer to the model, the two constants in the β function are optimized, as shown in Equation (6) (extracted from Equation (2)).

$$\beta = \beta_1 + \beta_2 \ln(N_f) = \frac{\sigma_{FL}\sqrt{\text{area}}^{1/6}}{(HV + 120)(\frac{1-R}{2})^{\alpha}} \tag{6}$$

The right-hand side of the equation is plotted against the lifetime (N_f) for all data points in Figure 19a,b and the two constants are extracted by linear regression to $\beta_1 = 3.93$ and $\beta_2 = -0.12$. The new fit is shown in Figure 19c,d.

From the results of the current article, it can be concluded that the size of the FGA, as well as the fish-eye area, is dependent on the material. The data on fracture initiation, hardness, and stress intensity in Figure 12 can be rearranged and the stress intensity at the fish-eye border plotted against hardness is shown in **Figure 20**, for the tested steel grades.

This indicates that the threshold value for the transition from fine flat crack propagation inside the fish eye to coarse crack propagation outside the fish eye is dependent on the mechanical properties of the material. The fish-eye threshold stress intensity
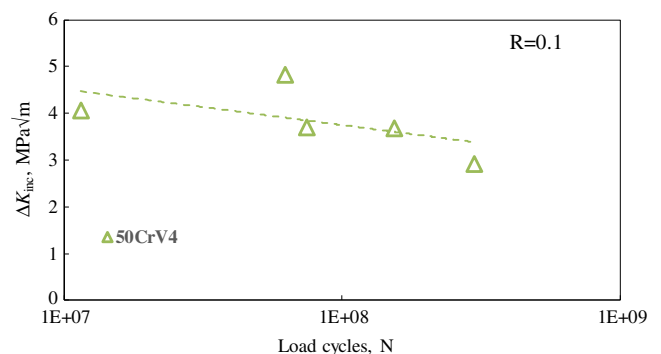

Figure 18. ΔK_{inc} plotted against fatigue life of 50CrV4, $K_t = 1.03$ at $R = 0.1$.

**ADVANCED
SCIENCE NEWS**

www.advancedsciencenews.com

**steel
research**
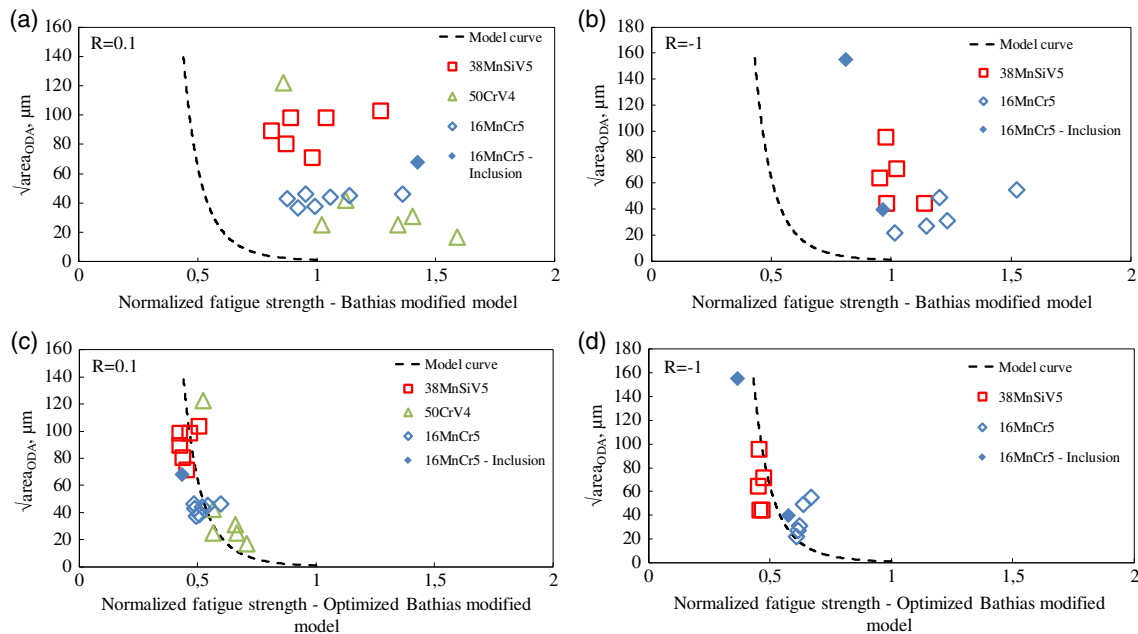international

www.steel-research.de

Figure 19. Model curve and experimental results with square root of ODA area plotted against normalized fatigue strength for $R = 0.1$ and $R = -1$ loading ratios. a,b) Bathias-modified Murakami model and c,d) Bathias-modified Murakami model with optimized β parameters.
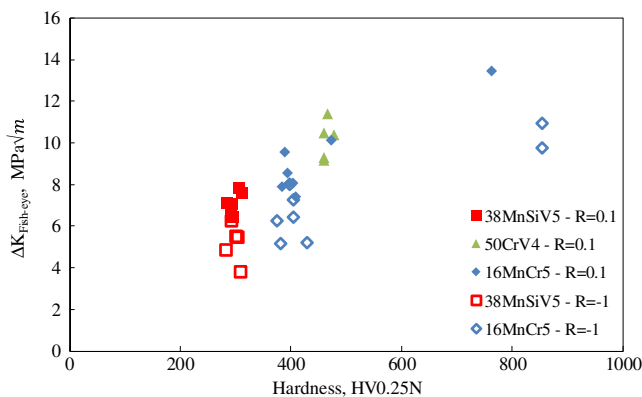

Figure 20. Relationship between fish-eye border effective stress intensities ($\Delta K_{eff} = K_{max}$-0), and steel hardness for $R = 0.1$ and $R = -1$.

increases with steel strength, suggesting a higher fracture energy in the coarser region and more ductile crack growth outside the fish eye. An increase in the mean load, i.e., from $R = -1$ to $R = 0.1$, leads to an increase in the threshold too.

FGA formation took readily place in all three grades, as shown in Figure 9–11, although with triple points acting as starting defects in the ferritic–pearlitic 38MnSiV5 grade and the more typical nonmetallic inclusions in the martensitic 50CrV4 and 16MnCr5 grades. It should be noted that FGA formation occurred in both $R = -1$ and $R = 0.1$ loading, as shown in Figure 13. FGA formation has been explained as due to polygonization and grain refinement in front of the crack tip.[13,22] Others proposed the grain refinement as due to the repeated collision between the crack surfaces during cyclic loading,[14] and hence proposed that no FGA formation occurs at positive

loading ratios, $R > 0$. However, in the results of the present work, and others,[16,17] FGA formation occurred under both $R = -1$ and $R = 0.1$ loading ratios.

The measured FGA sizes of failed specimen are on different levels between the three steel grades, as shown in Figure 13, and it illustrates a distinct dependence of the FGA sizes on the material properties. When taking the load into account and calculating the stress intensity factor at the FGA border, it is observed that the different FGA thresholds are close together seemingly independent of fatigue life, as shown in Figure 14. Combining the threshold data of FGAs and fish eyes and plotting against steel hardness, we obtain the image in **Figure 21**. The fish-eye thresholds are significantly dependent on hardness and higher than the FGA thresholds. The latter do not vary that much with hardness. Schematically, **Figure 22** is drawn. There is a baseline below which FGA crack growth prevails. Between the FGA baseline and the fish-eye threshold the fish-eye crack growth dominates and above there is the conventional fatigue crack propagation (FCP) region. The transition between the growth regions is controlled by the fracture mechanic's conditions, and it is dependent on material's strength.

The transition in the crack growth from FGA to fish-eye area is of particular interest as the crack growth within the FGA is ≈99% of the total lifetime, and thus the transition from FGA to fish eye is life limiting. The fracture surface inside the FGA is recognized by its unsmooth topography whereas outside the FGA and inside the fish eye a fine flat fracture surface is observed. It is safe to assume that the crack grows with much smaller increments while within the FGA than outside and that the crack tip plasticity increases with increasing crack length, as with increasing FGA size shown in Figure 15 and 16. Another assumption may be the transition in the crack growth mode that occurs when the crack tip plastic zone size in front of the crack tip covers a volume large
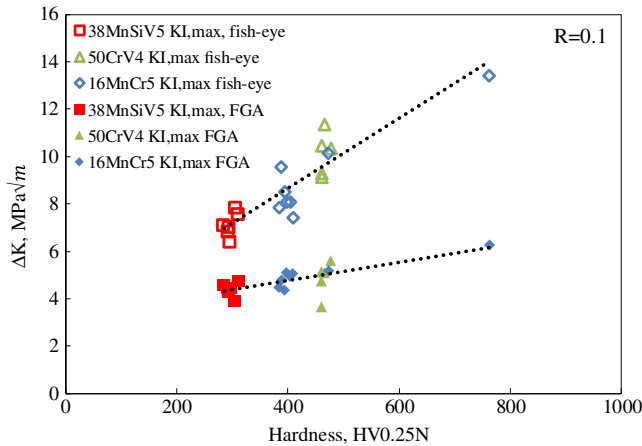
Figure 21. Threshold stress intensities $\Delta K_{fish-eye}$ and ΔK_{FGA} against steel grade hardnesses.
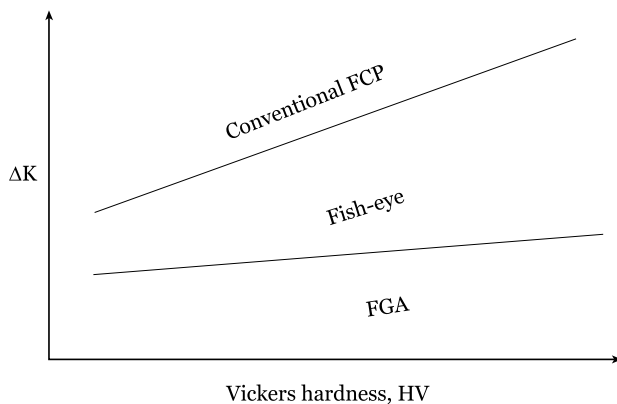

Figure 23. Hardness variability and indent plastic zone size H_p for the steel grades 38MnSiV5, 50CrV4, and 16MnCr5.

Figure 22. Schematic relation between FGA and fish-eye thresholds, material strength, and FCP regions.

Figure 24. Average plastic zone size at the FGA border and limiting indent plastic zone size.

enough to contain all microstructural varieties. This volume should be a material-specific volume, and it is demonstrated by the HV indent experiment shown in Figure 17. The plastic zone size beneath an indent is treated in several studies.[32–36] Here, we will use the approximate slip cone model,[33] where the plastic zone size H_p is related to indent depth t

$$\frac{t}{H_p} = 0.172 \tag{7}$$

The indent depth is derived from the indent diagonal measurements. Thus, Figure 17 may be transformed to the hardness variability versus the indent plastic zone size in **Figure 23**. A measure of when the hardness variability levels of is arbitrarily taken where the gradient is −0.001 similar for the three grades. The corresponding indent plastic zone sizes (at 5.3%, 4.3%, and 2.7% hardness variability for 38MnSiV5, 16MnCr5, and 50CrV4, respectively) are considered material-specific measures of when the plastic deformation becomes independent of the microstructure variations. Next, the plastic zone sizes at FGA
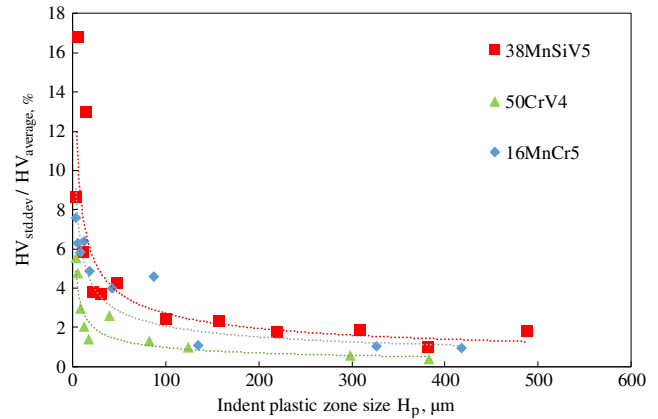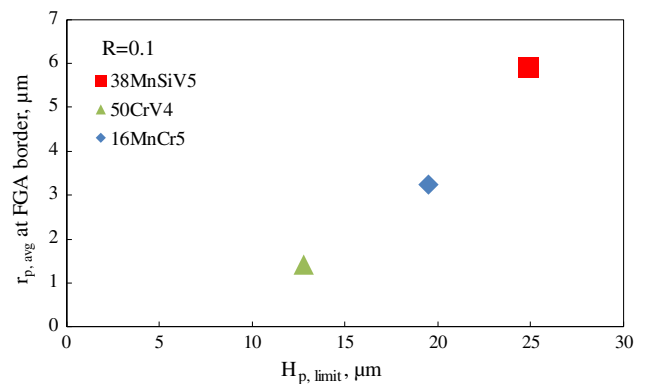
are plotted against the specific indent plastic zone sizes, as shown in **Figure 24**.

The limiting indent plastic zone size does not translate directly to the FGA plastic zone size, as there is a scaling conversion between crack tip plasticity and indent plasticity, but it shows the relation between the critical FGA plastic zone size to a material-specific plastic zone size dependent on microstructure. When the FGA plastic zone size is below the limiting condition, the crack growth is in the FGA region, and when it is above, it will jump into the fish-eye region.

The threshold values for FGA formation in high-strength steels were proposed in previous studies[3,16] to be related to the Irwin plastic zone size at the crack tip and the "characteristic material length scale" (l_m) introduced in another previous study.[37]

$$l_m = b \left(\frac{G}{\sigma_y} \right)^2 \tag{8}$$

where b is the burgers vector, G is the shear modulus, and σ_y is the yield strength. The FGA formation is assumed complete when the plastic zone size equals the characteristic material

**ADVANCED
SCIENCE NEWS**

www.advancedsciencenews.com

**steel
research**
international

www.steel-research.de

Table 5. Comparison of proposed parameters and experimental results of the present study.

Grade	r_p, μm, Exp.	l_m, μm, Eq. 7	$H_{p,limit}$, μm, Exp.	K_{FGA}, MPa√m, Eq. 8	K_{FGA}, MPa√m, $R = 0.1$, Exp.
38MnSiV5	5.9	4.7	24.9	5.5	4.39
16MnCr5	3.3	2.1	19.5	5.5	5.02
50CrV4	1.4	0.92	12.8	5.5	4.86

length ($r_y = l_m$). Using Equation (5) and (8), the stress intensity factor at this specific point is

$$K_{FGA,I} = G\sqrt{6\pi \boldsymbol{b}} \tag{9}$$

K_{FGA} is also related to, according to previous studies[3,16], the material crack growth threshold stress intensity K_{th}.

A comparison of the parameters of Equation (8) and (9) to the present experimental results is shown in **Table 5**. The characteristic material length scale is l_m in Equation (8), the experimental limiting indent plastic zone size is $H_{p,limit}$, the stress intensity factor at the FGA border (K_{FGA}) is shown in Equation (9), and the experimental stress intensity factor (K_{FGA}) is shown at the FGA border. The <111> burgers vector for the tested steels was assumed as 2.49 Å.

The plastic zone size r_p relates well to l_m and also to $H_{p,limit}$ but with other scaling. The l_m is based on the parameters of plastic shear, shear modulus, and yield limit, whereas $H_{p,limit}$ is based on a concept of microstructural variation, but still both relates similarly to r_p. The magnitude of the model FGA and the experimental FGA stress intensities agrees well, whereas the latter varies with strength but not the former. Thus, the conditions controlling the transition of FGA into fish-eye crack growth have been illuminated. Further studies to clarify the crack growth within the FGA are of high interest.

5. Conclusions

Fatigue strength and SN curves in the VHCF regime of three high-strength microalloyed steel grades were determined and the influence of mean load and notch on the fatigue strength was demonstrated. Fractography analysis of the failed specimens was conducted, where the investigation of crack initiation mechanisms was performed. The following conclusions were drawn from the results of this study.

1) All three investigated bar grades displayed a finite fatigue life up to 10^9 load cycles, although with a quite flat SN curve between 10^6 and 10^9 load cycles. 2) The influence of mean load on fatigue strength, obtained by staircase testing, seems to follow a Goodman relation. One staircase test series, out of nine, failed due to surface defects and reduced fatigue strength results. 3) The influence of the notch was negligible regarding the ferritic–pearlitic steel; in the martensitic 50CrV4, there was a slight increase in fatigue strength, and there was a decrease in carburized steel. 4) Both interior and surface failure initiations occurred depending on the presence of initiation defects, local strength (in the carburized case), and stress distribution. FGA

and fish-eye formation occurred in all three steel grades. Material mechanical properties have a clear effect on the size of the FGA and fish-eye regions. 5) Controlling conditions for the transition between FGA, fish-eye, and conventional crack growth regions were explored by crack tip plastic zone size and stress intensity estimates at the FGA and fish-eye transitions. Hardness mapping was related to the FGA transition crack tip plastic zone size to overcome a volume of microstructural variation. Schematic descriptions are given.

Conflict of Interest

The authors declare no conflict of interest.

[1] S. Bergamo, in *VHCF5-Fifth Int. Conf. on Very High Cycle Fatigue*, **2011**.

[2] J. Bergström, N. Hallbäck, M. Sadek, C. Burman, S. Plano, B. Weber, S. Mustermann, K. Gillner, O. Polit, L. Gallimard, T. Palin-Luc, M. Ouarabi, K.-H. Lang, S. Becker, R. E. Eguizabal, B. Escauriaza, in *Influence of Cycling Frequency on Fatigue Strength and Crack Growth of Engineering Steels for Demanding APPLICATIONS (FREQTIGUE)*, **2018**.

[3] I. Marines, G. Dominguez, G. Baudry, J. F. Vittori, S. Rathery, J. P. Doucet, C. Bathias, *Int. J. Fatigue* **2003**, *25*, 1037.

[4] M. Sadek, in *A Study on the Comings of the VHCF and the Testing Technique and Equipment Within*, **2020**.

[5] H. Mughrabi, *Fatigue Fract. Eng. Mater. Struct.* **2002**, *25*, 755.

[6] H. Mughrabi, *Procedia Eng.* **2013**, *55*, 636.

[7] H. Mughrabi, *Int. J. Fatigue* **2006**, *28*, 1501.

[8] C. Bathias, *Fatigue Fract. Eng. Mater. Struct.* **1999**, *22*, 559.

[9] A. Giertler, U. Krupp, *Procedia Struct. Integr.* **2016**, *2*, 1207.

[10] U. Krupp, A. Giertler, K. Koschella, *Procedia Eng.* **2016**, *160*, 231.

[11] I. Marines-Garcia, P. C. Paris, H. Tada, C. Bathias, *Mater. Sci. Eng.: A* **2007**, *468–470*, 120.

[12] I. Marines-Garcia, P. C. Paris, H. Tada, C. Bathias, D. Lados, *Eng. Fract. Mech.* **2008**, *75*, 1657.

[13] V. Kazymyrovych, J. Bergström, C. Burman, *Steel Res. Int.* **2010**, 308.

[14] A. Zhao, J. Xie, C. Sun, Z. Lei, Y. Hong, *Int. J. Fatigue* **2012**, *38*, 46.

[15] K. Shiozawa, T. Hasegawa, Y. Kashiwagi, L. Lu, *Int. J. Fatigue* **2009**, *31*, 880.

[16] M. W. Tofique, J. Bergström, K. Svensson, *Int. J. Fatigue* **2017**, *100*, 238.

[17] V. Kazymyrovych, J. Ekengren, J. Bergström, C. Burman, in *Fourth Int. Conf. on Very High Cycle Fatigue (VHCF-4)*, **2007**.

**ADVANCED
SCIENCE NEWS**

www.advancedsciencenews.com

**steel
research**
international

www.steel-research.de

[18] C. Bathias, P. C. Paris, *Gigacycle Fatigue in Mechanical Practice*, Marcel Dekker, New York, USA **2005**.

[19] Y. Furuya, *Mater. Sci. Eng.: A* **2011**, *528*, 5234.

[20] H.-P. Gaenser, *Comput. Mater. Sci.* **2008**, *44*, 230.

[21] J. Bergström, V. Kasymyrovych, C. Burman, J. Ekengren, in *5th Int. Conf. on Very High Cycle Fatigue (VHCF-5)*, **2011**.

[22] W. Li, T. Sakai, Q. Li, L. T. Lu, P. Wang, *Mater. Sci. Eng.: A* **2011**, *528*, 5044.

[23] Y. Murakami, T. Nomoto, T. Ueda, *Fatigue Fract. Eng. Mater. Struct.* **1999**, *22*, 581.

[24] Y. Murakami, *Int. J. Fatigue* **2012**, *41*, 2.

[25] Y. Murakami, Y. Yamashita, *Procedia Eng.* **2014**, *74*, 6.

[26] Y.-L. Lee, *Fatigue Testing and Analysis: Theory and Practise*, Elsevier Butterworth-Heinemann, Amsterdam, Netherlands **2005**.

[27] W. J. Dixon, A. M. Mood, *J. Am. Stat. Assoc.* **1948**, *43*, 109.

[28] SS-ISO_12107, *Metallic Materials – Fatigue Testing – Statistical Planning and Analysis of Data*, Sweden **2012**.

[29] R. W. Hertzberg, R. P. Vinci, J. L. Hertzberg, *Deformation and Fracture Mechanics of Engineering Materials*, John Wiley & Sons **2012**.

[30] T. L. Anderson, *Fracture Mechanics: Fundamentals and Applications*, Taylor & Francis, CRC Press **2017**.

[31] U. Krupp, A. Giertler, K. Koschella, *Fatigue Fract. Eng. Mater. Struct.* **2017**, *40*, 1731.

[32] M. Mata, O. Casals, J. Alcalá, *Int. J. Solids Struct.* **2006**, *43*, 5994.

[33] A. Udalov, S. Parshin, *Mater. Today: Proc.* **2019**.

[34] K. L. Johnson, *J. Mech. Phys. Solids* **1970**, *18*, 115.

[35] R. F. Bishop, R. Hill, N. F. Mott, *Proc. Phys. Soc.* **1945**, *57*, 147.

[36] R. Hill, *The Mathematical Theory of Plasticity*, Oxford University Press **1950**.

[37] W. D. Nix, H. Gao, *J. Mech. Phys. Solids* **1998**, *46*, 411.

2000060 (13 of 13)